



MECA0010 - Uncertainty quantification and stochastic modeling - Assignment 2

Brandoit Julien s200710

This work is part of the MECA0010 course but is a further exploration of the work I am performing in my master's thesis: *Design of a deep neural network for parameter estimation in high dimensional conductance-based models* [tentative title].

Academic year 2024-2025

Introduction

Computational neuroscience uses mathematical models to understand the brain's functioning, physiology, development, and cognition. These models facilitate the application of numerical tools to explore the complex, hierarchical, and non-linear nature of biological systems.

One important branch focuses on cellular-level modeling, including both single-cell models and models of neural networks. Among these, *conductance-based models* are particularly prominent for several reasons:

- **Accurate representation of experimental phenomena**, such as action potentials, oscillations, and precise responses to stimuli, by incorporating ion channels and their dynamic properties.
- **Direct physiological interpretations**, linking model parameters (such as conductances and time constants) to measurable biological properties, bridging theory and experimentation.
- **Historical significance**, with the pioneering Hodgkin-Huxley model (1952) establishing the foundation for computational neuroscience, earning the Nobel Prize in 1963 [8, 1].
- **Flexibility**, allowing the integration of new ion channels, adaptation mechanisms, or other cellular processes for a wide range of biological questions.

However, these models also face notable challenges:

- **Complexity in modeling additional currents**, as new currents introduce new parameters and interactions that complicate model dynamics.
- **High dimensionality**, as increasing model complexity can lead to an overwhelming number of parameters, making analysis and optimization difficult.
- **Degeneracy**, where multiple parameter sets can lead to similar behaviors, complicating the interpretation and validation of models.

These challenges have contributed to a decline in experimentalists' interest in conductance-based models. Nevertheless, recent advances, particularly the concept of *dynamic input conductances* (DICs), offer promising solutions to these issues.

Problem Formulation

Conductance-Based Models

Conductance-based models describe the system dynamics via a set of ODEs for the state variables:

$$\mathbf{x} = [V, m_1, h_1, m_2, h_2, \dots, m_N, h_N, \lambda_1, \lambda_2, \dots, \lambda_M]$$

Here, V represents the membrane potential, m_i are activation variables, h_i are inactivation variables, and λ_j represent ionic or neuromodulator concentrations. The model is governed by:

$$C\dot{V} = I_{\text{ext}}(t) - \sum_{i=1}^N I_i - g_{\text{leak}}(V - E_{\text{leak}}), \quad I_i = \bar{g}_i m_i^p h_i^q (V - E_i) \quad (1)$$

$$\tau_{m_i}(V, \boldsymbol{\lambda}) \dot{m}_i = m_{\infty, i}(V, \boldsymbol{\lambda}) - m_i, \quad \tau_{h_i}(V, \boldsymbol{\lambda}) \dot{h}_i = h_{\infty, i}(V, \boldsymbol{\lambda}) - h_i \quad (2)$$

$$\tau_{\lambda_j}(V, \boldsymbol{\lambda}) \dot{\lambda}_j = f_{\lambda_j}(t, V, \boldsymbol{\lambda}, \mathbf{m}, \mathbf{h}) \quad (3)$$

The membrane potential dynamics are influenced by ion currents, with the gating of ion channels modeled by activation and inactivation variables. The leak current is also included, and external current $I_{\text{ext}}(t)$ may be injected into the system. The activation and inactivation variables follow first-order dynamics, while the ionic and neuromodulator concentrations have more varied dynamics.

The Stomatogastric Ganglion Neuron

This study focuses on the STG neuron model from [10], refined in subsequent works [7, 5]. The model includes 7 ionic currents and leak current, with calcium dynamics explicitly described, notably for the I_{KCa} current. The membrane potential is given by:

$$\begin{aligned} C\dot{V} = & - \left(\bar{g}_{\text{Na}} m_{\text{Na}}^3 h_{\text{Na}} (V - E_{\text{Na}}) + \bar{g}_{\text{Kd}} m_{\text{Kd}}^4 (V - E_{\text{K}}) + \bar{g}_{\text{CaT}} m_{\text{CaT}}^3 h_{\text{CaT}} (V - E_{\text{Ca}}) \right. \\ & + \bar{g}_{\text{CaS}} m_{\text{CaS}}^3 h_{\text{CaS}} (V - E_{\text{Ca}}) + \bar{g}_{\text{KCa}} m_{\text{KCa}}^4 (V - E_{\text{K}}) + \bar{g}_{\text{A}} m_{\text{A}}^3 h_{\text{A}} (V - E_{\text{K}}) \\ & \left. + \bar{g}_{\text{H}} m_{\text{H}} (V - E_{\text{H}}) + g_{\text{leak}} (V - E_{\text{leak}}) \right). \end{aligned}$$

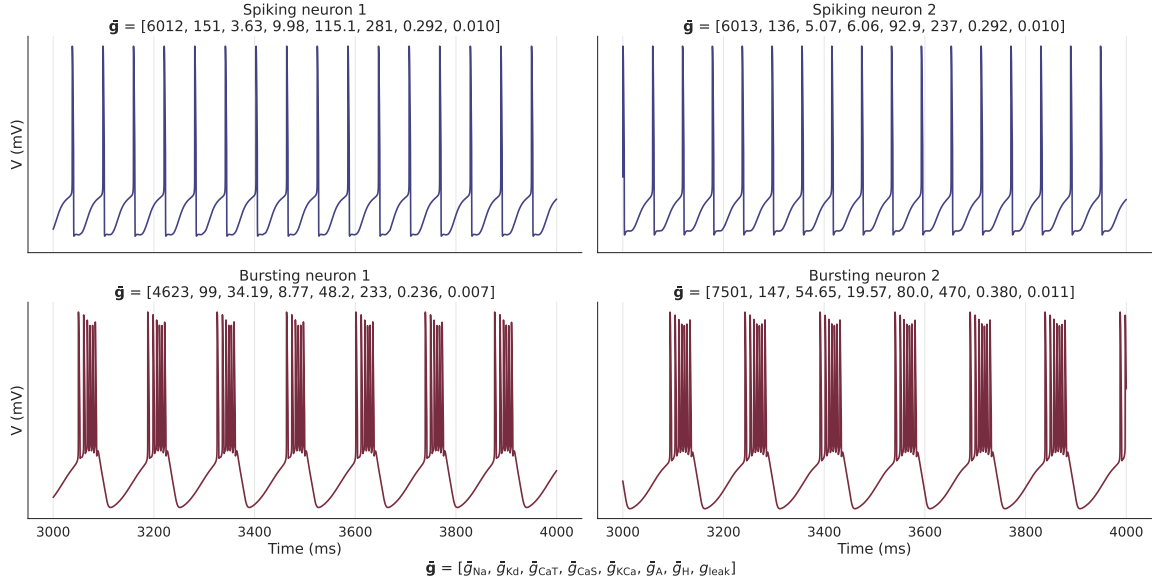


Figure 1: Illustration of intrinsic behaviors in the STG neuron model. The top row shows spiking behavior, and the bottom row shows bursting behavior. These behaviors demonstrate degeneracy, where different parameter sets lead to similar dynamics.

A complete presentation of the model and equations is provided in the appendix for the more curious reader. In the absence of external current, the neuron's stationary behavior is determined by the maximum conductances:

$$\bar{\mathbf{g}} = [\bar{g}_{\text{Na}}, \bar{g}_{\text{Kd}}, \bar{g}_{\text{CaT}}, \bar{g}_{\text{CaS}}, \bar{g}_{\text{KCa}}, \bar{g}_{\text{A}}, \bar{g}_{\text{H}}, g_{\text{leak}}].$$

Distinct behaviors, such as *spiking* and *bursting*, are observed. Figure 1 illustrates these behaviors and demonstrates the phenomenon of *degeneracy*, where different parameter sets produce similar dynamics [6, 11, 5].

Dynamic Input Conductances

Dynamic Input Conductances (DICs), introduced in [2] following [3, 4], offer a framework for understanding neuronal behavior. Instead of focusing on the exact values of maximal conductances, DICs aggregate the contributions of various channels across different timescales. This degeneracy arises because the neuron's intrinsic behavior is determined by the aggregation of these channels, not their exact values. Thus, any conductance-based model can be described by DICs rather than by the vector $\bar{\mathbf{g}}$. Mathematically, it can be written:

$$g_f(V) = \frac{1}{g_{\text{leak}}} \left[\frac{\partial \dot{V}}{\partial V} + \sum_{i=1}^N w_{\text{fs}}^{X_i} \left(\frac{\partial \dot{V}}{\partial X_i} \frac{\partial X_{i,\infty}}{\partial V} \right) \right] \quad (4)$$

$$g_s(V) = \frac{1}{g_{\text{leak}}} \left[\sum_{i=1}^N (w_{\text{su}}^{X_i} - w_{\text{fs}}^{X_i}) \left(\frac{\partial \dot{V}}{\partial X_i} \frac{\partial X_{i,\infty}}{\partial V} \right) \right] \quad (5)$$

$$g_u(V) = \frac{1}{g_{\text{leak}}} \left[\sum_{i=1}^N (1 - w_{\text{su}}^{X_i}) \left(\frac{\partial \dot{V}}{\partial X_i} \frac{\partial X_{i,\infty}}{\partial V} \right) \right] \quad (6)$$

Here, $w_{\text{fs}}^{X_i}$ and $w_{\text{su}}^{X_i}$ are voltage-dependent weights that modulate the contribution of X_i to fast (f), slow (s), and ultraslow (u) timescales based on the logarithmic differences in time constants.

Degeneracy arises because the neuron's intrinsic behavior is determined by the DICs, not the exact values of maximal conductances. As shown in [2, 5], this degeneracy holds around $V_{\text{th}} \approx -51$ mV, where the DICs can fully describe the system's behavior. The neurons in Fig. 1 have different $\bar{\mathbf{g}}$ values but similar \mathbf{g}_{DICs} : spiking neurons: $g_f = -6.6$, $g_s = 4$, $g_u = 5$, and bursting neurons: $g_f = -6.6$, $g_s = -4$, $g_u = 5$. This reduces the dimensionality of the STG model from 8 variables to just 3:

$$\bar{\mathbf{g}} \in \mathbb{R}_+^8 \xrightarrow{\text{DICs}} \mathbf{g}_{\text{DICs}}(V_{\text{th}} \approx -51\text{mV}) = [g_f(V_{\text{th}}), g_s(V_{\text{th}}), g_u(V_{\text{th}})] \in \mathbb{R}^3$$

In the remainder of this work, reference is made to DICs at V_{th} .

Research Question

This work focuses on quantifying the impact of the values of \bar{g} on the resulting g_{DICs} . Specifically, it is assumed that the values of \bar{g} are uncertain—reflecting the scenario where an experimenter works with neurons in a laboratory—and aim to evaluate how this uncertainty propagates across different timescales. This question is addressed through Monte Carlo simulations and a stochastic sensitivity analysis.

The DICs are treated as a black-box model, meaning that while it can compute g_{DICs} for a given set of \bar{g} , the explicit computational details remain inaccessible. Figure 2 provides a synthesis of the methodological pipeline used in this work.

The remainder of this report is organized as follows: It is first presented the assumed distributions for maximal conductances and the hypotheses underlying the pipeline. Then, Monte Carlo simulations are conducted to generate a large number of samples. Finally, a preliminary analysis of the estimated distributions of g_{DICs} is performed, followed by a more detailed sensitivity analysis using variance decomposition. A convergence analysis is carried out to provide credibility to the results obtained from the Monte Carlo simulations, both for the sample-based distributions and the sensitivity indices.

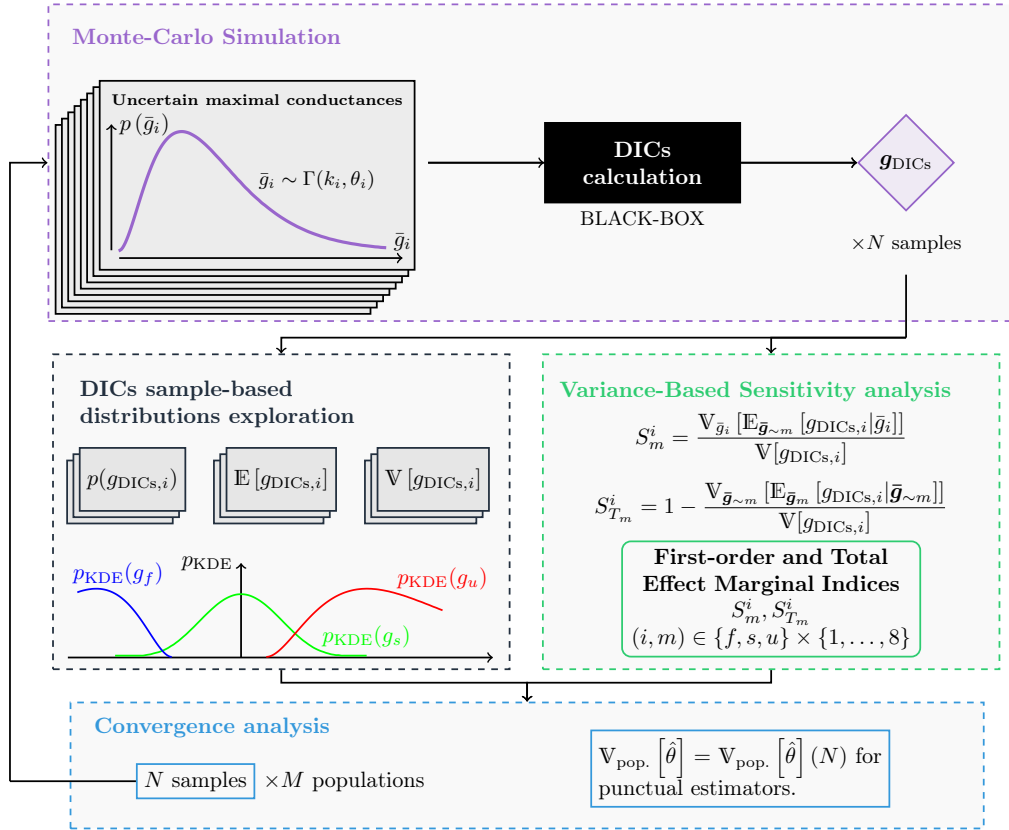


Figure 2: *Illustrative pipeline of the methodology utilized in this report.* The framework begins with uncertain maximal conductances, modeled as Gamma distributions, denoted by $\bar{g}_i \sim \Gamma(k_i, \theta_i)$. These are sampled across multiple Monte Carlo simulations to compute DICs (g_{DICs}) through a black-box calculation. The sampled DICs are further explored through KDE-based distribution estimation (p_{KDE}) to derive summary statistics (mean, variance) and analyze distribution characteristics. Variance-based sensitivity analysis quantifies the influence of parameters on outputs using Sobol indices and total effect indices. Convergence analysis is performed on the punctual estimators, as well as on the sensitivity indices, by examining variances across populations as a function of the population size. This integrative approach systematically assesses uncertainty propagation, sensitivity, and estimator convergence.

Monte Carlo simulation

The results of this work are generated numerically using Monte Carlo simulations. A *population* is generated, defined as a set of N *samples* drawn from the assumed probability distributions of the maximum conductances. These samples are fed into the black box, and a set of N model outputs corresponding to the input samples is obtained.

The sampling method used in this work is a naive method—i.e., no quasi-random sampling methods such as *Latin hypercube sampling* or *Sobol Sampling* are employed. This choice is made to maintain simplicity, owing

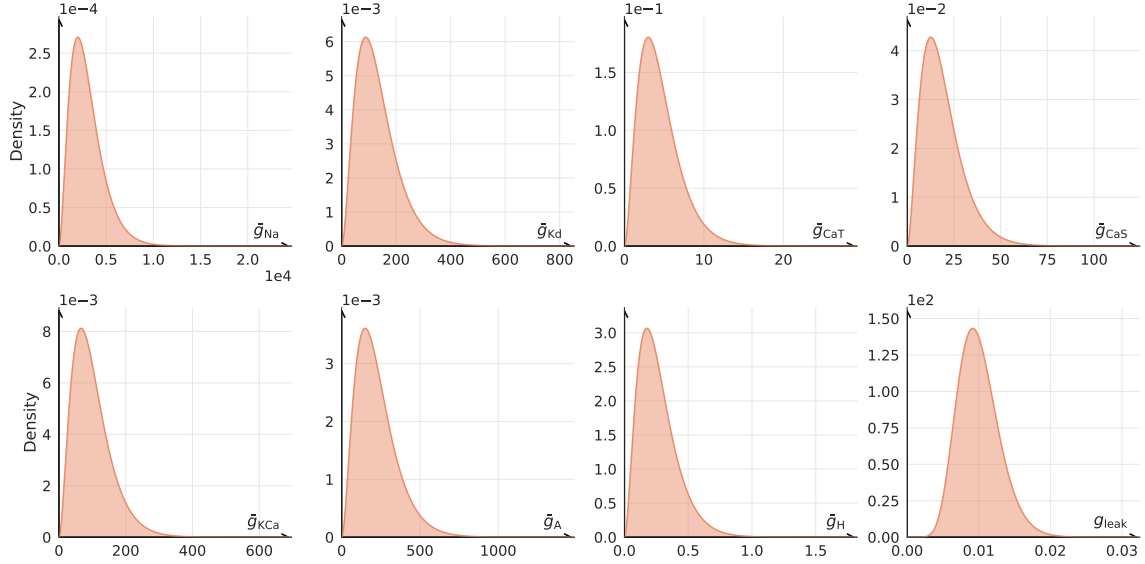


Figure 3: Illustration of the probability distributions for the maximum conductances. The distributions are derived from Gamma distributions (Eq. (8)), which incorporate widely accepted biological priors. The figure demonstrates that the majority of the probability mass is concentrated in a range similar to that in previous studies [5], while ensuring that there is no upper bound on the support.

to both the simplicity and the low computational cost of evaluating the black box. From a technical point of view, the black box was implemented from scratch, as was the Monte Carlo method.

Modeling the Uncertainty of Maximum Conductances

In order to represent the uncertainty of the maximum conductances, it is necessary to choose a probability distribution $p(\bar{\mathbf{g}})$. There is no consensus in the literature on which distribution to use or even on the existence of a maximum bound on its support. [10] use uniform distributions, while [5] employs a hierarchical construction of uniform distributions, resulting in bounded-support (truncated) exponential-like distributions that are non-independent.

This work adopts the approach of encoding widely accepted biological priors, while avoiding placing an arbitrary upper bound on the support. The maximum conductances are assumed to be independent for three main reasons: 1. This allows the use of simpler sensitivity analysis tools; 2. The dependence between the expression of different ion channels has not reached consensus in the literature; 3. If such a dependence exists, it arises from complex biochemical mechanisms acting on timescales not considered in this study (further details can be found in [10], which proposes adding a very slow dynamics for $\bar{\mathbf{g}}$). This independence can be written as:

$$p(\bar{\mathbf{g}}) = p(\bar{g}_{Na}, \bar{g}_{Kd}, \bar{g}_{CaT}, \bar{g}_{CaS}, \bar{g}_{KCa}, \bar{g}_A, \bar{g}_H, g_{leak}) = p(\bar{g}_{Na})p(\bar{g}_{Kd}) \dots p(g_{leak}) \quad (7)$$

The two widely accepted biological priors are: 1. The maximum conductance is a concentration of channels at the surface of the cell membrane, so $\bar{g}_{ion} \geq 0$; 2. While there is no strict upper bound on the number of channels at the membrane, a very large number of channels is unlikely, as is a number close to zero. A similar idea can be expressed for the leak conductance. The choice of Gamma distributions allows us to incorporate these two priors.

$$\bar{g}_i \sim \Gamma(k_i, \theta_i), \quad f_{\bar{g}_i}(x) = \frac{1}{\Gamma(k_i)\theta_i^{k_i}} x^{k_i-1} \exp\left(-\frac{x}{\theta_i}\right), \quad x \in [0, +\infty[\quad (8)$$

The shape parameters k_i and scale parameters θ_i are determined such that the first and second moments of the Gamma distributions match those of the uniform distributions proposed in [5]. Table (Appendix, 3) summarizes the parameters obtained after matching the moments. Figure 3 illustrates the distributions.

Dynamic Input Conductances Distributions

This section examines the distributions of the Dynamic Input Conductances (DICs) obtained after propagating the uncertainty of the maximal conductances $\bar{\mathbf{g}}$ through the black-box model. Utilizing 300,000 Monte Carlo simulations, the resulting samples of the DICs are generated, representing the model outputs under the given uncertainties in the input parameters. Although the outputs are probably interdependent, it is chosen to study each output separately (through marginal distributions) and leave the quantification of dependencies for future works. A similar approach is used in sensitivity analysis.

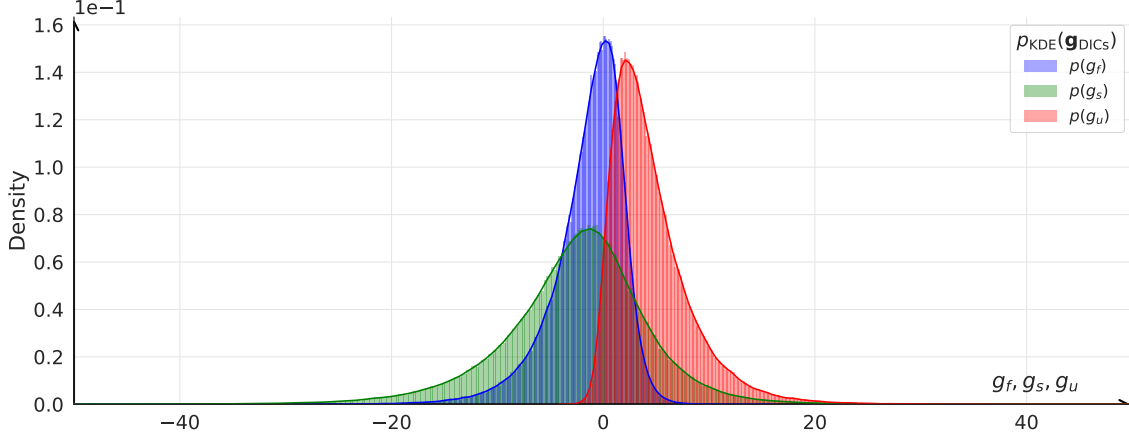


Figure 4: The distributions of the Dynamic Input Conductances (DICs) are obtained through 300,000 Monte Carlo simulations using the black-box model. The resulting samples of the DICs are then analyzed using Kernel Density Estimation (KDE) with Gaussian Kernels with the Scott bandwidth method [13] to estimate the marginal distributions for g_f , g_s , and g_u . These distributions represent the uncertainty propagation across the different conductance parameters.

The distributions of the DICs are analyzed using Kernel Density Estimation (KDE) with Gaussian kernels, applying the Scott bandwidth method [13]. The KDE estimation allows us to estimate the marginal distributions of the fast DIC g_f , the slow DIC g_s , and the ultra-slow DIC g_u . The results are shown in Fig. 4.

The observed distributions of the DICs spread across a range of values, confirming that uncertainty in the maximal conductances \bar{g} directly impacts the values of the DICs. More specifically:

- The fast DIC g_f mostly span over the negative range even if small positive values are possible. This is consistent with biological observations of fast feedback that is mainly positive (upstroke of the spike) [a positive feedback is characterized by a negative conductance].
- The slow DIC g_s cover both positive and negative values in a relatively symmetrical and centered way. This result is also consistent with biological observations of slow feedback (downstroke of the spike), the sign of which determines the type of behavior.
- The ultra-slow DIC g_u cover positive values, which is also consistent with biological interpretations.

Only a few samples seem to cover non-physiological values [3, 4, 2], which lends considerable credence to this STG model, which gives physiological results over the whole parameter space associated with plausible maximal conductances distributions. This is really interesting from a computational neuroscience point of view.

Table 1 below summarizes the key statistics of the DICs distributions, including the mean, standard deviation (std), and a 95% mass interval for each of the three DICs (g_f , g_s , g_u).

DIC Type	Mean	Standard Deviation	95% Mass Interval
Fast DIC g_f	-1.44	3.48	[-9.98, 3.51]
Slow DIC g_s	-2.59	6.96	[-18.17, 10.28]
Ultra-slow DIC g_u	4.54	3.82	[-0.18, 14.23]

Table 1: Summary statistics of the Dynamic Input Conductances distributions: mean, standard deviation, and a 95% mass interval for each DIC (g_f , g_s , and g_u). In particular, the mass intervals are within plausible ranges [3, 4, 2].

Stochastic Global Sensitivity Analysis

A global sensitivity analysis was conducted to evaluate the impact of maximal conductances on model output variability using Sobol sensitivity indices [14]. First-order indices (S_i) measure the variance explained by individual parameters, while total indices (S_{T_i}) [9] account for both direct and interactive effects.

The theoretical formulations of the indices and their Monte Carlo estimators are presented below. In practice,

a custom implementation was performed—no external sensitivity analysis library was used.

$$S_i = \frac{\mathbb{V}_{\bar{g}_i} [\mathbb{E}_{\bar{g}_{\sim i}} [Y | \bar{g}_i]]}{\mathbb{V}[Y]} \xrightarrow{\text{MC estimator}} \frac{\frac{1}{N} \sum_{k=1}^N [Y_{B,k} (Y_{A_i,k} - Y_{A,k})]}{\frac{1}{N-1} \sum_{k=1}^N (Y_{A,k} - \bar{Y}_A)^2} \quad (9)$$

$$S_{T_i} = 1 - \frac{\mathbb{V}_{\bar{g}_{\sim i}} [\mathbb{E}_{\bar{g}_i} [Y | \bar{g}_{\sim i}]]}{\mathbb{V}[Y]} \xrightarrow{\text{MC estimator}} \frac{\frac{1}{2} \frac{1}{N} \sum_{k=1}^N [(Y_{A,k} - Y_{A_i,k})^2]}{\frac{1}{N-1} \sum_{k=1}^N (Y_{A,k} - \bar{Y}_A)^2} \quad (10)$$

In these formulations, Y_A , Y_B , and Y_{A_i} represent the outputs computed for sets A , B , and A_i , respectively. $A, B, A_i \in \mathbb{R}^{N \times 8}$. The estimators follow the method described by [12], but unlike that study, a classical (random) Monte Carlo sampling approach was used instead of quasi-random sampling. While this approach may slow convergence, the results obtained are correct. Convergence analysis was performed to validate the results. For index estimation, 300,000 samples were generated and divided between two sets A and B . Crossed sets A_i were then constructed for each parameter i by replacing column i of A with that of B .

The computed Sobol indices are summarized in Table 2. The first-order indices indicate that the maximal conductances \bar{g}_{Na} , \bar{g}_{CaS} , \bar{g}_A , and \bar{g}_H are the parameters with the most significant direct impact on the variance of the model outputs.

The maximal conductance \bar{g}_{Na} primarily influences the variance of the fast DIC, g_f , while \bar{g}_{CaS} and \bar{g}_A mainly affect the slow DIC, g_s . Meanwhile, the variance of the ultra-slow DIC, g_u , is predominantly determined by \bar{g}_H and g_{leak} . The results also show that the sum of first-order indices approaches 90%, suggesting that the majority of the output variance can be attributed to individual parameter contributions.

Although \bar{g}_{leak} has a low first-order index, its total index is significant, indicating that its impact is primarily through nonlinear interactions with other parameters. This reflects a partially additive structure in the model, where key interactions are centered around the leak conductance. This near-additive model structure is confirmed by the sum of total indices approaching 1 [9].

This type of sensitivity analysis is particularly important in experimental contexts where data are scarce and costly to collect, as is often the case in neuronal studies. By targeting the most influential parameters identified by this analysis, it becomes possible to optimize experimental design by prioritizing the calibration of maximal conductances \bar{g}_{Na} , \bar{g}_{CaS} , \bar{g}_A , \bar{g}_H , and g_{leak} . This approach maximizes the information gained while minimizing the number and cost of required experiments. Identifying these parameters could suffice to significantly reduce overall uncertainty.

Two additional observations can be made: while approximately 10% of the variance remains unexplained by first-order effects, which may be significant in many engineering domains, this fraction can be considered small in the context of experimental cellular biology. Finally, this sensitivity analysis is distribution-dependent, and the qualitative results (which conductances are most important) are likely more robust than the quantitative results (what fraction of variance is explained), as the distribution of \bar{g} is likely far more complex than that used in this study.

Output	\bar{g}_{Na}	\bar{g}_{Kd}	\bar{g}_{CaT}	\bar{g}_{CaS}	\bar{g}_{KCa}	\bar{g}_A	\bar{g}_H	g_{leak}	$\sum_m(\cdot)$
$S_m^{g_f}$ (First Order)	0.79	0.00	0.00	0.00	0.00	0.05	0.04	0.05	0.94
$S_m^{g_s}$ (First Order)	0.00	0.00	0.01	0.59	0.00	0.33	0.00	0.03	0.95
$S_m^{g_u}$ (First Order)	0.00	0.00	0.00	0.01	0.00	0.01	0.76	0.14	0.92
$S_{T_m}^{g_f}$ (Total)	0.85	0.00	0.00	0.00	0.00	0.05	0.04	0.13	1.07
$S_{T_m}^{g_s}$ (Total)	0.00	0.00	0.01	0.61	0.00	0.35	0.00	0.10	1.07
$S_{T_m}^{g_u}$ (Total)	0.00	0.00	0.00	0.01	0.00	0.01	0.81	0.22	1.05

Table 2: Sobol indices for maximal conductances \bar{g}_i (inputs), grouped by output variables g_f , g_s , and g_u . The rightmost column shows the sums of indices (S_m^i for first order and $S_{T_m}^i$ for total indices) for each output. Indices contributing more than 10% of the variance are considered significant.

Convergence Analysis

This final section aims to provide credibility to the results presented in this work. No additional information on the dynamics of ion channels or DICs will be detailed here. The objective is to provide evidence supporting the convergence of the estimators obtained via Monte Carlo methods. Specifically, the convergence of the means, standard deviations, and interval bounds of the masses detailed in Table 1 is analyzed. The convergence of these estimators serves as evidence for the convergence of the complete KDE estimators presented in Fig. 4. Additionally, the convergence of the Sobol indices presented in Table 2 is also examined.

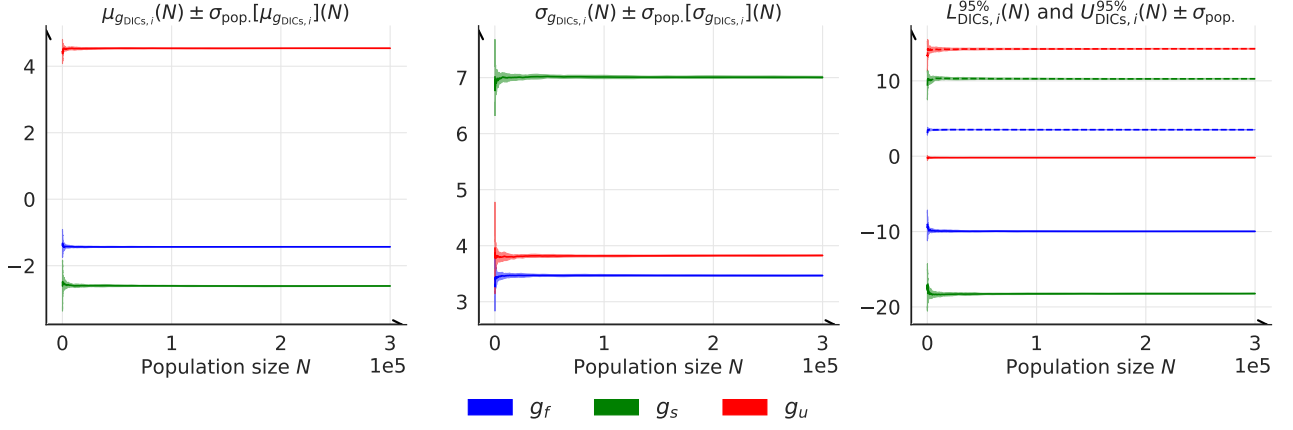


Figure 5: Convergence analysis of the estimators shown in Table 1. The mean of the estimators across $M = 16$ independent populations is represented as mean \pm standard deviation of the estimator across populations. The analysis is conducted as a function of the number of independent samples N that constitute the populations.

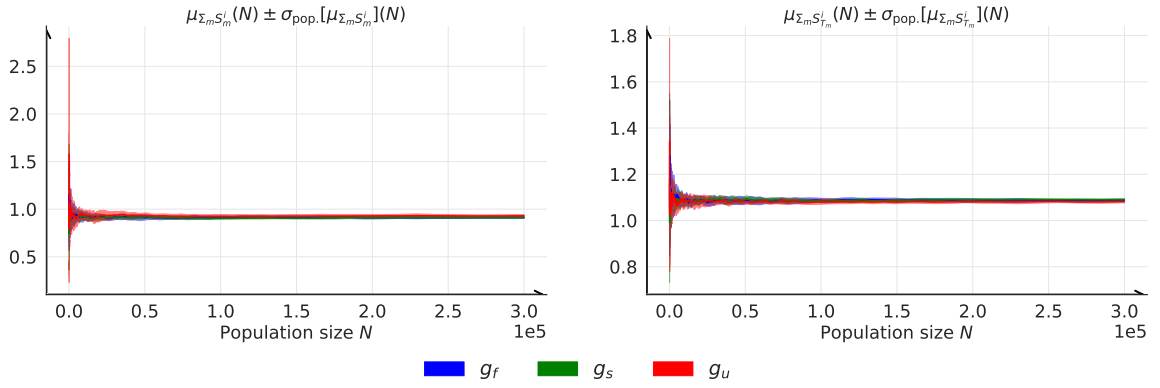


Figure 6: Convergence analysis of the sums presented in Table 2. The mean of the estimators across $M = 16$ independent populations is represented as mean \pm standard deviation of the estimator across populations. The analysis is conducted as a function of the number of independent samples N that constitute the populations. For an analysis of all estimators, please refer to Fig. (Appendix, 7a and 7b).

The methodology used is summarized in Fig. 2. In particular, the simplicity of evaluating the black box is leveraged to quickly generate numerous independent samples in various independent simulations. The variance of the estimators is assessed across different simulations (populations) as well as its evolution with respect to the number of samples within each population. The law of large numbers guarantees a decrease in variance as the number of samples increases (assuming that it can be applied). A graphical analysis of this variance is provided. The argument for convergence is that if the variance across simulations is low for a given population size, the estimator is well-converged for that population size, regardless of the specific population. The numerical analysis compares 16 independent populations. The implementation of this convergence analysis was also carried out from scratch.

Figure 5 illustrates the convergence of the estimators listed in Table 1. Figure 6 illustrates the convergence of the sum of the Sobol indices. Combined with Figures (Appendix, 7a) and (Appendix, 7b), it demonstrates the convergence of the estimators listed in Table 2. For all estimators, it is observed that for 300,000 samples, the variance across populations is relatively low. This result justifies the population size used in this work. For a numerical value of the standard deviation of the estimators for $N = 300,000$, refer to Table (Appendix, 4).

References

- [1] A. F. Huxley A. L. Hodgkin and J. Eccles. *Nobel Prize in Physiology or Medicine 1963*. <https://www.nobelprize.org/prizes/medicine/1963/>. Accessed: 2024-12-06. 1963.
- [2] Guillaume Drion et al. “Dynamic Input Conductances Shape Neuronal Spiking”. In: *eNeuro* 2.1 (2015). eCollection 2015 Jan-Feb, ENEURO.0031–14.2015. ISSN: 2373-2822. DOI: 10.1523/ENEURO.0031-14.2015. URL: <https://doi.org/10.1523/ENEURO.0031-14.2015>.
- [3] Alessio Franci, Guillaume Drion, and Rodolphe Sepulchre. “An organizing center in a planar model of neuronal excitability”. In: *SIAM Journal on Applied Dynamical Systems* 11.4 (2012), pp. 1698–1722. DOI: 10.1137/120875016.
- [4] Alessio Franci et al. “A balance equation determines a switch in neuronal excitability”. In: *PLoS Computational Biology* 9.3 (2013), e1003040. DOI: 10.1371/journal.pcbi.1003040.
- [5] Arthur Fyon et al. “Dimensionality reduction of neuronal degeneracy reveals two interfering physiological mechanisms”. In: *PNAS Nexus* 3.10 (Sept. 2024), pgae415. ISSN: 2752-6542. DOI: 10.1093/pnasnexus/pgae415.
- [6] Jean-Marc Goaillard and Eve Marder. “Ion Channel Degeneracy, Variability, and Covariation in Neuron and Circuit Resilience”. In: *Annual Review of Neuroscience* 44 (2021), pp. 335–357. DOI: 10.1146/annurev-neuro-092920-121538.
- [7] R. M. Harris-Warrick et al. *Dynamic Biological Networks: The Stomatogastric Nervous System*. Cambridge, MA: MIT Press, 1992.
- [8] A. L. Hodgkin and A. F. Huxley. “A Quantitative Description of Membrane Current and its Application to Conduction and Excitation in Nerve”. In: *Journal of Physiology* 117.4 (1952), pp. 500–544. DOI: 10.1113/jphysiol.1952.sp004764.
- [9] T. Homma and A. Saltelli. “Importance measures in global sensitivity analysis of nonlinear models”. In: *Reliability Engineering and System Safety* 52 (1996), pp. 1–17.
- [10] Zheng Liu et al. “A Model Neuron with Activity-Dependent Conductances Regulated by Multiple Calcium Sensors”. In: *Journal of Neuroscience* 18.7 (1998), pp. 2309–2320. DOI: 10.1523/JNEUROSCI.18-07-02309.1998.
- [11] Uta Noppeney, Karl J. Friston, and Cathy J. Price. “Degenerate neuronal systems sustaining cognitive functions”. In: *Journal of Anatomy* 205.6 (2004), pp. 433–442. DOI: <https://doi.org/10.1111/j.0021-8782.2004.00343.x>.
- [12] A. Saltelli et al. *Global Sensitivity Analysis. The Primer*. Chichester, UK: John Wiley & Sons, 2008.
- [13] D. W. Scott. *Multivariate Density Estimation: Theory, Practice, and Visualization*. New York, Chichester: John Wiley & Sons, 1992.
- [14] I. M. Sobol. “Global sensitivity indices for nonlinear mathematical models and their Monte Carlo estimates”. In: *Mathematics and Computers in Simulation* 55.1-3 (2001), pp. 271–280. DOI: 10.1016/S0378-4754(00)00270-6.

Appendices

A Detailed Description of the STG Neuron Model

The stomatogastric ganglion (STG) neuron model employed in this study is based on the formulation introduced by [10] with refinements from subsequent studies. The model is characterized by seven ionic currents in addition to the leak current, with no external current applied. Below, we detail the components and equations governing the model:

A.1 Membrane Potential Dynamics

The membrane potential V evolves according to the following equation:

$$C\dot{V} = - (g_{Na}m_{Na}^3h_{Na}(V - E_{Na}) + g_{Kd}m_{Kd}^4(V - E_K) + g_{CaT}m_{CaT}^3h_{CaT}(V - E_{Ca}) + g_{CaS}m_{CaS}^3h_{CaS}(V - E_{Ca}) + g_{KCa}m_{KCa}^4(V - E_K) + g_Am_A^3h_A(V - E_K) + g_Hm_H(V - E_H) + g_{leak}(V - E_{leak})),$$

where $C = 1$ is the membrane capacitance, g_i represents the maximal conductances, and E_i denotes the reversal potentials for the respective ionic currents.

A.2 Gating Variables

The dynamics of the activation (m) and inactivation (h) gating variables are described by:

$$\tau_{m,i}(V)\dot{m}_i = m_{\infty,i}(V) - m_i, \quad \tau_{h,i}(V)\dot{h}_i = h_{\infty,i}(V) - h_i, \quad (11)$$

where $\tau_{m,i}(V)$ and $\tau_{h,i}(V)$ are voltage-dependent time constants, and $m_{\infty,i}(V)$ and $h_{\infty,i}(V)$ are steady-state activation and inactivation functions, respectively.

The specific definitions of these functions for different ion channels are as follows:

- Sodium (Na):

$$m_{\infty,Na}(V) = \frac{1}{1 + \exp((V + 25.5)/-5.29)},$$

$$h_{\infty,Na}(V) = \frac{1}{1 + \exp((V + 48.9)/5.18)},$$

$$\tau_{m,Na}(V) = 1.32 - 1.26 \exp((V + 120)/-25),$$

$$\tau_{h,Na}(V) = (0.67 \exp((V + 62.9)/-10)) \times (1.5 \exp((V + 34.9)/3.6)).$$

- Potassium Delayed Rectifier (Kd):

$$m_{\infty,Kd}(V) = \frac{1}{1 + \exp((V + 12.3)/-11.8)},$$

$$\tau_{m,Kd}(V) = 7.2 - 6.4 \exp((V + 28.3)/-19.2).$$

- Calcium T-Type (CaT):

$$m_{\infty,CaT}(V) = \frac{1}{1 + \exp((V + 27.1)/-7.2)},$$

$$h_{\infty,CaT}(V) = \frac{1}{1 + \exp((V + 32.1)/5.5)},$$

$$\tau_{m,CaT}(V) = 21.7 - 21.3 \exp((V + 68.1)/-20.5),$$

$$\tau_{h,CaT}(V) = 105 - 89.8 \exp((V + 55)/-16.9).$$

- Calcium Slow (CaS):

$$m_{\infty,CaS}(V) = \frac{1}{1 + \exp((V + 33)/-8.1)},$$

$$h_{\infty,CaS}(V) = \frac{1}{1 + \exp((V + 60)/6.2)},$$

$$\tau_{m,CaS}(V) = 1.4 + \frac{7}{\exp((V + 27)/10) + \exp((V + 70)/-13)},$$

$$\tau_{h,CaS}(V) = 60 + \frac{150}{\exp((V + 55)/9) + \exp((V + 65)/-16)}.$$

- Potassium Calcium-Dependent (KCa):

$$m_{\infty,KCa}(V, [Ca^{2+}]) = \frac{[Ca^{2+}]}{[Ca^{2+}] + 3} \cdot \frac{1}{1 + \exp((V + 28.3)/-12.6)},$$

$$\tau_{m,KCa}(V) = 90.3 - 75.1 \exp((V + 46)/-22.7).$$

- A-Type Potassium (A):

$$m_{\infty,A}(V) = \frac{1}{1 + \exp((V + 27.2)/-8.7)},$$

$$h_{\infty,A}(V) = \frac{1}{1 + \exp((V + 56.9)/4.9)},$$

$$\tau_{m,A}(V) = 11.6 - 10.4 \exp((V + 32.9)/-15.2),$$

$$\tau_{h,A}(V) = 38.6 - 29.2 \exp((V + 38.9)/-26.5).$$

- Hyperpolarization-Activated Current (H):

$$m_{\infty,H}(V) = \frac{1}{1 + \exp((V + 70)/6)},$$

$$\tau_{m,H}(V) = 272 + 1499 \exp((V + 42.2)/-8.73).$$

The Nernst Potential are :

- $E_{leak} = -50mV$
- $E_{Na} = 50mV$
- $E_K = -80mV$
- $E_H = -20mV$
- $E_{Ca} = 80mV$

A.3 Calcium Dynamics

Calcium dynamics play a critical role in the STG model. The intracellular calcium concentration $[Ca^{2+}]$ influences calcium-dependent potassium currents (I_{KCa}) and follows:

$$\tau_{Ca} \frac{d[Ca^{2+}]}{dt} = -\alpha_{Ca} (I_{CaT} + I_{CaS}) + \beta_{Ca}, \quad (12)$$

where $\alpha_{Ca} = 0.94$, $\beta_{Ca} = 0.05$, and $\tau_{Ca} = 20$ ms is the calcium decay time constant.

B Parameter Distributions for Monte Carlo Simulations

The maximal conductances (g_i) are treated as random variables following Gamma distributions to encode biological priors:

$$g_i \sim \Gamma(k_i, \theta_i), \quad (13)$$

where k_i and θ_i are shape and scale parameters, respectively. Table 3 summarizes the parameterization used in this study, derived from moment-matching of uniform distributions in previous literature [5].

Maximal conductances	Uniform range, adapted from [5]	Shape parameters k_i	Scale parameters θ_i
\bar{g}_{Na}	[0, 6000.0]	3.0	1000.0
\bar{g}_{Kd}	[0, 265]	3.0	44.1667
\bar{g}_{CaT}	[0, 9.0]	3.0	1.5
\bar{g}_{CaS}	[0, 38]	3.0	6.3333
\bar{g}_{KCa}	[0, 200]	3.0	33.3333
\bar{g}_{A}	[0, 450.0]	3.0	75.0
\bar{g}_{H}	[0, 0.53]	3.0	0.0883
g_{leak}	[0.005, 0.015]	12.0	0.000833

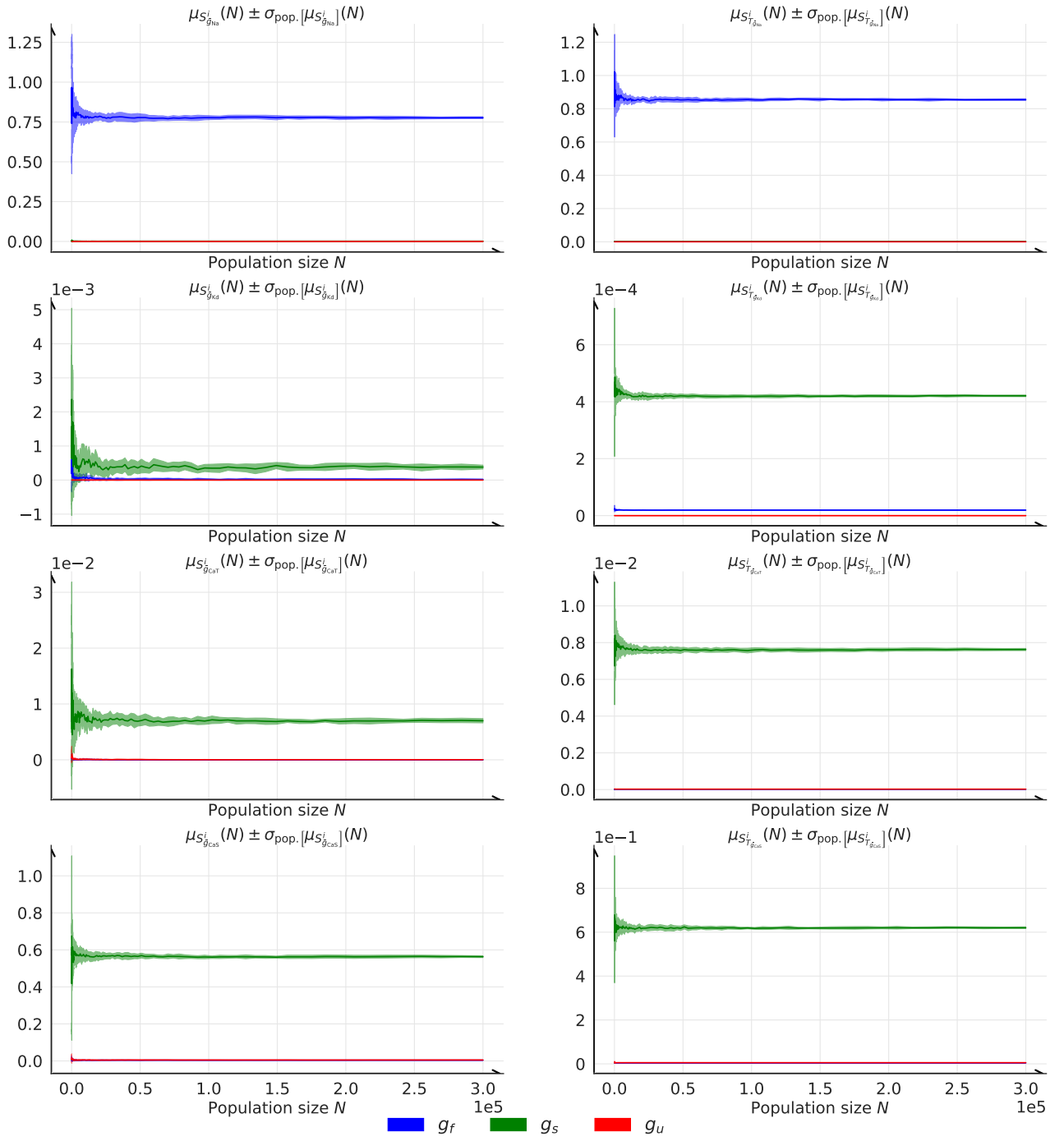
Table 3: Parametrizations of the maximal conductances \bar{g}_i for various ion channels, showing their uniform ranges (adapted from [5]). The corresponding shape (k_i) and scale (θ_i) parameters of the Gamma distributions are derived via moment matching, where $k_i = \frac{3(a+b)^2}{(b-a)^2}$ and $\theta_i = \frac{(b-a)^2}{6(a+b)}$, with a and b being the bounds of the uniform distribution. One can refer to Fig. 3 to visualize the resulting distributions.

C Additional Figures and Table

Figures below summarize key results from the study.

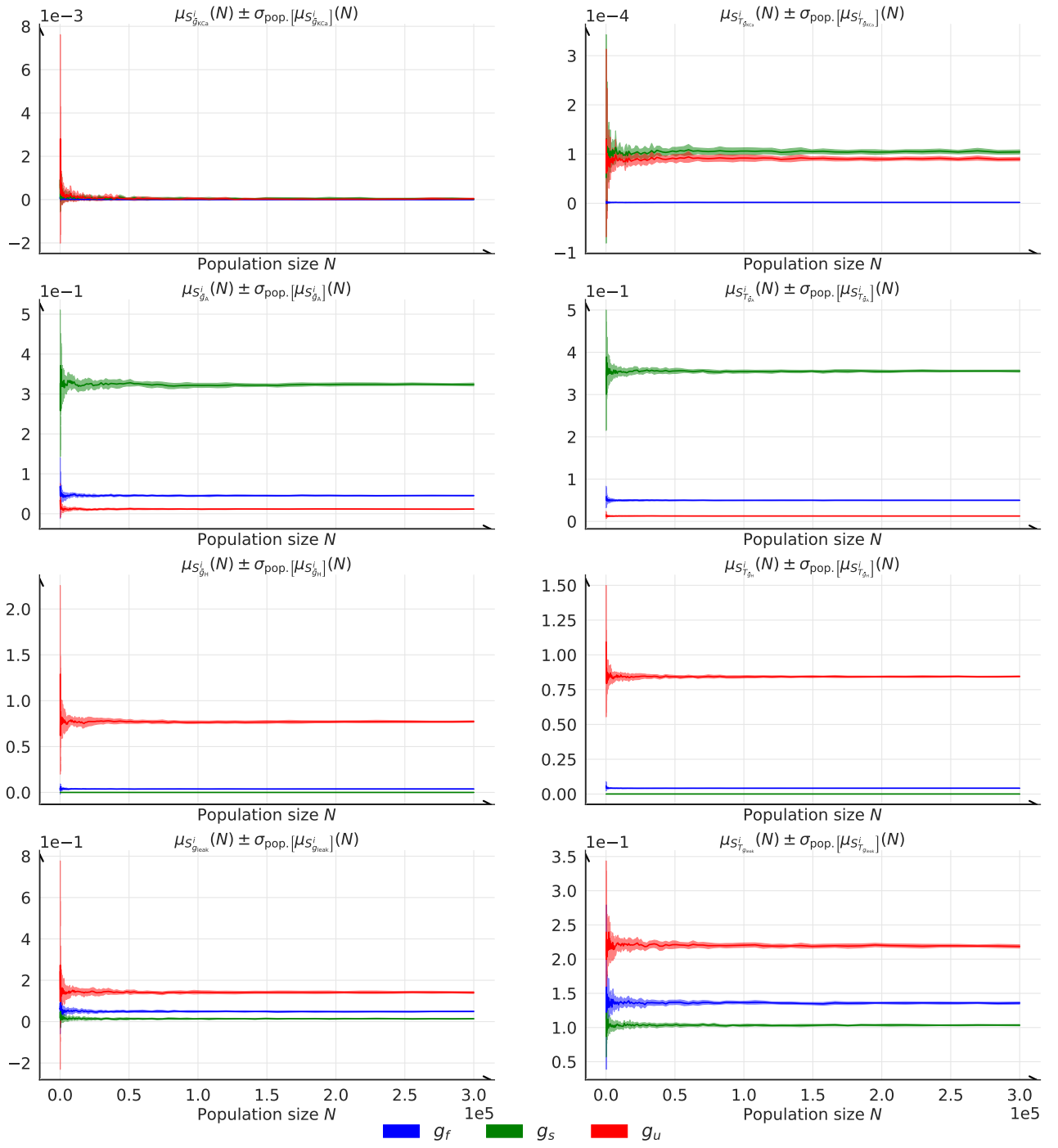
	g_f	g_s	g_u
<i>Table 1</i>			
Mean of DICs	4.491×10^{-3}	1.163×10^{-2}	5.233×10^{-3}
Std of DICs	5.764×10^{-3}	1.771×10^{-2}	8.672×10^{-3}
95% Mass Interval of DICs			
$\left[L^{95\%} \right]$	$\left[2.67 \times 10^{-2} \right]$	$\left[5.13 \times 10^{-2} \right]$	$\left[6.80 \times 10^{-3} \right]$
$\left[U^{95\%} \right]$	$\left[6.77 \times 10^{-3} \right]$	$\left[4.63 \times 10^{-2} \right]$	$\left[3.51 \times 10^{-2} \right]$
<i>Table 2</i>			
Sum of First Order Indices	1.147×10^{-2}	5.601×10^{-3}	1.390×10^{-2}
Sum of Total Indices	7.908×10^{-3}	3.655×10^{-3}	5.279×10^{-3}
$S_{\bar{g}_{Na}}^i$	9.509×10^{-3}	1.176×10^{-4}	0.000
$S_{\bar{g}_{Kd}}^i$	1.324×10^{-5}	7.077×10^{-5}	0.000
$S_{\bar{g}_{CaT}}^i$	1.291×10^{-5}	3.525×10^{-4}	2.190×10^{-5}
$S_{\bar{g}_{CaS}}^i$	2.097×10^{-4}	3.943×10^{-3}	3.808×10^{-4}
$S_{\bar{g}_{KCa}}^i$	1.844×10^{-6}	2.877×10^{-5}	2.383×10^{-5}
$S_{\bar{g}_A}^i$	8.126×10^{-4}	2.873×10^{-3}	5.941×10^{-4}
$S_{\bar{g}_H}^i$	6.022×10^{-4}	0.000	1.177×10^{-2}
$S_{\bar{g}_{leak}}^i$	2.160×10^{-3}	1.509×10^{-3}	4.683×10^{-3}
$S_{T_{\bar{g}_{Na}}}^i$	6.773×10^{-3}	7.065×10^{-6}	0.000
$S_{T_{\bar{g}_{Kd}}}^i$	1.736×10^{-7}	2.897×10^{-6}	0.000
$S_{T_{\bar{g}_{CaT}}}^i$	1.107×10^{-7}	5.450×10^{-5}	1.668×10^{-7}
$S_{T_{\bar{g}_{CaS}}}^i$	2.957×10^{-5}	2.655×10^{-3}	5.428×10^{-5}
$S_{T_{\bar{g}_{KCa}}}^i$	8.221×10^{-8}	4.163×10^{-6}	3.993×10^{-6}
$S_{T_{\bar{g}_A}}^i$	4.630×10^{-4}	2.838×10^{-3}	1.503×10^{-4}
$S_{T_{\bar{g}_H}}^i$	3.790×10^{-4}	0.000	5.361×10^{-3}
$S_{T_{\bar{g}_{leak}}}^i$	1.587×10^{-3}	7.822×10^{-4}	1.771×10^{-3}

Table 4: Standard deviations of estimators between $M = 16$ independent populations for $N = 300,000$ independent samples. This corresponds to the final standard deviation in Fig. 5, Fig. 6, Fig. (Appendix, 7a) and Fig. (Appendix, 7b). All these standard deviations are small, which lends support to the convergence of the results presented.



(a) First part of Fig. 7

Figure 7: Continued on the next page.



(b) Second part of Fig. 7

Figure 7: Convergence analysis of the estimators shown in Table 2. We represent the mean of the estimators between $M = 16$ independent populations \pm the standard deviation of this estimator between populations. Analysis as a function of the number of independent samples N that constitute the populations.